

LETTER TO THE EDITOR

Stray light correction and contrast analysis of Hinode broad band images

S. K. Mathew^{1,2}, V. Zakharov², and S. K. Solanki^{2,3}

¹ Udaipur Solar Observatory, P. O. Box 198, Udaipur - 313004, India

e-mail: shibu@prl.res.in

² Max-Planck-Institut für Sonnensystemforschung (MPS), Max-Planck-Str. 2, 37191 Katlenburg-Lindau, Germany

e-mail: zakharov@mps.mpg.de, solanki@mps.mpg.de

³ School of Space Research, Kyung Hee University, Yongin, Gyeonggi 446-701, Korea

Received; accepted

ABSTRACT

The contrasts of features in the quiet Sun are studied using filtergrams recorded by the Broad-band Filter Imager on the Hinode/Solar Optical Telescope. In a first step, the scattered light originating in the instrument is modeled using Mercury transit data. Combinations of four two-dimensional Gaussians with different widths and weights were employed to retrieve the point-spread functions (PSF) of the instrument at different wavelengths, which also describe instrumental scattered light. The parameters of PSFs at different wavelengths are tabulated. The observed images were then deconvolved using the PSFs. The corrected images were used to obtain contrasts of features such as bright points and granulation in different wavelength bands. After correction, *rms* contrasts of the granulation of between 0.11 (at 668 nm) and 0.22 (at 388 nm) are obtained. Similarly, bright point contrasts ranging from 0.07 (at 668 nm) to 0.78 (at 388 nm) are found, which are a factor of 1.8 to 2.8 higher than those obtained before PSF deconvolution. The mean contrast of the bright points is found to be somewhat higher in the CN-band than in the G-band, which confirms theoretical predictions.

Key words. Sun: granulation – Sun: photosphere – instrumentation: high angular resolution

1. Introduction

The contrast of granulation and of magnetic features is an important diagnostic of their thermal structure and provides insight into the energy transport mechanisms acting in them. The contrast of granulation, bright points and other small scale features is influenced by the point spread function (PSF), the width of whose core is a measure of the spatial resolution, while the strength of the wings is determined by the amount of light scattered within the instrument (or in the atmosphere, if present). In particular, the scattered light strongly reduces the contrast. Bright points, which are smaller in size than the granules, are more strongly affected. If the PSF is known, then it can be used to deconvolve the observed image and thus to approximately retrieve the original intensities.

Contrasts measured with the Hinode Solar Optical Telescope (SOT, Tsuneta et al. 2008, Suematsu et al. 2008, Kosugi et al. 2007) are of particular interest due to the combination of high spatial resolution and the absence of seeing, leading to almost constant observing conditions. The value of the Hinode SOT observations would be further enhanced if the PSF could be determined and compensated for (e.g. as done by Mathew, et al. 2007 for MDI continuum images).

The PSF of the Hinode Spectro Polarimeter (SP) was determined by Danilovic et al. (2008) by modeling the SOT/SP optical system using the ZEMAX optical design software. After convolving solar granulation data from MHD simulations with

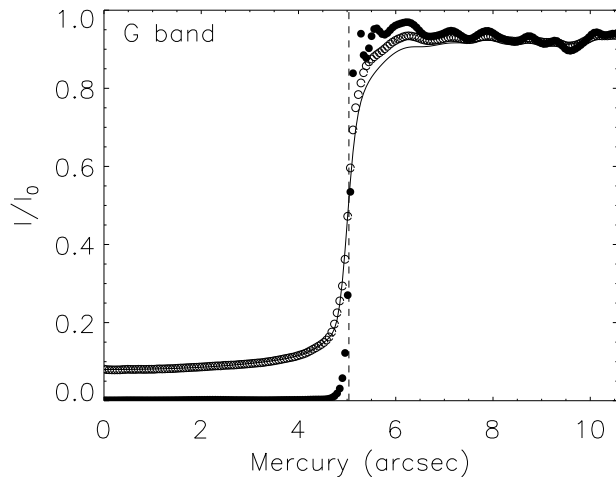
the computed PSF, they found that the *rms* contrast of the simulated granulation matches closely the observations from SOT/SP. Wedemeyer-Böhm (2008) used Mercury transit and eclipse images to obtain the PSF of the Hinode/SOT/Broadband Filter Imager (BFI) instrument, but did not apply the obtained PSF to deducing the true contrast in the BFI wavelength bands. In this paper we obtain the PSF of the Hinode/SOT/BFI instrument also using observed Mercury transit images, but following the approach successfully applied to MDI images by Mathew et al. (2007). We use the retrieved PSF for the deconvolution of the images observed with the Hinode/SOT/BFI instrument to recover the original intensities. In Sect. 2 we describe the method used for the retrieval of the PSF. In Sect. 3 we present initial results showing the difference in granulation contrast before and after the image correction. Conclusions are given in Sect. 4.

2. Image correction

We used images recorded on 8th Nov. 2006 during a Mercury transit to obtain the PSF of the instrument. Full pixel resolution (0.05448 arcsec/pixel) images in the CN and G-bands and also in blue, green and red continuum bands were available. The theoretical resolution (λ/D) of the Hinode/SOT ranges from 0.16 to 0.28 arc-sec between the CN-band and red continuum wavelengths. In the absence of instrumental scattered light Mercury should appear completely black, whereas in the observations it obviously is not (Fig. 1). The open circles in Fig. 1 indicate the radial (azimuthally averaged) intensity profile of Mercury observed in the G-band, which shows a scattered light level of around 7 - 8% near the center of Mercury's disk. Significant stray

Table 1. Retrieved parameters for four-Gaussian PSFs. Width is specified in arc-secs.

Wavelength (Å)	Gaussian I		Gaussian II		Gaussian III		Gaussian IV	
	weight	width	weight	width	weight	width	weight	width
3883 (CN)	0.6489	0.1084	0.1794	0.5158	0.1152	1.6999	0.0565	18.907
4305 (GB)	0.6392	0.1250	0.1721	0.5329	0.1014	1.8076	0.0873	19.047
4504 (BC)	0.6423	0.1390	0.1748	0.5212	0.1050	1.6844	0.0780	19.173
5550 (GC)	0.6250	0.1960	0.1698	0.6505	0.0920	1.6888	0.1131	18.686
6684 (RC)	0.6228	0.2188	0.1601	0.8181	0.0927	1.8330	0.1243	19.018

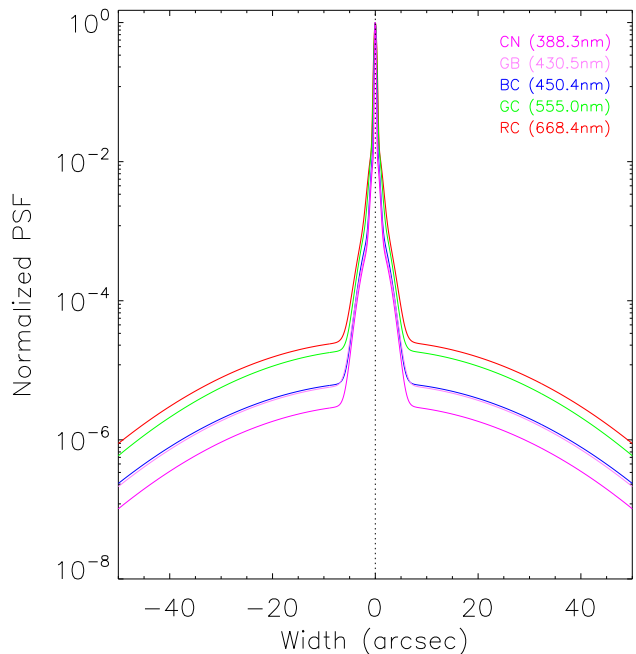
**Fig. 1.** The fit to the radially averaged Mercury intensity profile. Open circles outline the observed intensity profile, the solid line represents the fit to the observed profile and filled circles follow the intensity profile after correction. The vertical dashed line marks Mercury's limb. The ripples in the intensity profile outside Mercury's image are mainly due to the average intensity variations in the granules.

light is also found at all the other wavelengths, with an increase in the scattered light level from shorter to longer wavelengths (see the additional electronic material for similar plots at other wavelengths; Fig. A.1).

In order to obtain the PSF of the instrument we proceeded as follows. The intensity values within the image of Mercury were replaced by zeros. These images were convolved with a guess PSF, generated by a combination of four two-dimensional Gaussians. It was found that the use of four Gaussians, instead of three Gaussians and a Lorentzian as used in Mathew et al. (2007) for MDI full-disk images, gave a better fit in our case i.e. for the Mercury transit images. The Gaussians with appropriate weights and widths are representative of both the diffraction limited PSF and the non-ideal part which contributes to the scattered light in the instrument. By performing a two-dimensional convolution we make sure that the stray light from all sides contributes to the intensity within Mercury's image. The sum of the two-dimensional Gaussians used for the convolution is,

$$PSF = \sum_{i=1}^4 w_i c_i e^{-x^2/(2b_i^2)}$$

where b_i is the width, $c_i = 1/2\pi b_i^2$ the normalization constant and w_i the weight of the i -th Gaussian. The radial profile of the azimuthally averaged intensity within Mercury's outline from

**Fig. 2.** PSF for different wavelengths observed by Hinode/SOT/BFI. The corresponding values for the weights and widths of the Gaussian functions are given in table 1.

the convolved images was iteratively fit to the similarly averaged observed intensity. The solid line in Fig. 1 shows the best fit to the azimuthally averaged intensity profile through the G-band Mercury image. Figure 2 shows the normalized PSF for different wavelengths observed with Hinode/SOT/BFI. The weights and widths of the two-dimensional Gaussian functions are listed in Table 1. The narrowest Gaussian in all cases closely reproduces the theoretical resolution of the telescope, while the remaining Gaussians with broader widths mainly account for the scattered light in the telescope.

In the next step, the best-fit parameters were used to retrieve the stray light-free intensities from the observed images. As pointed out by Wedemeyer-Bhöm (2008) the scattering could be anisotropic and the resulting PSF could be different for observations from different fields-of-views. Since we assume that the scattering is uniform within the observed field-of-view, we restrict our contrast analysis to around the same part of the image, where the Mercury transit observations were obtained, but avoid the immediate vicinity of Mercury's image to avoid being influenced by artifacts of the deconvolution.

The restoration of the images was carried out using the maximum likelihood deconvolution method (an IDL routine available in Astrolib is used for this purpose, Richardson 1972, Lane

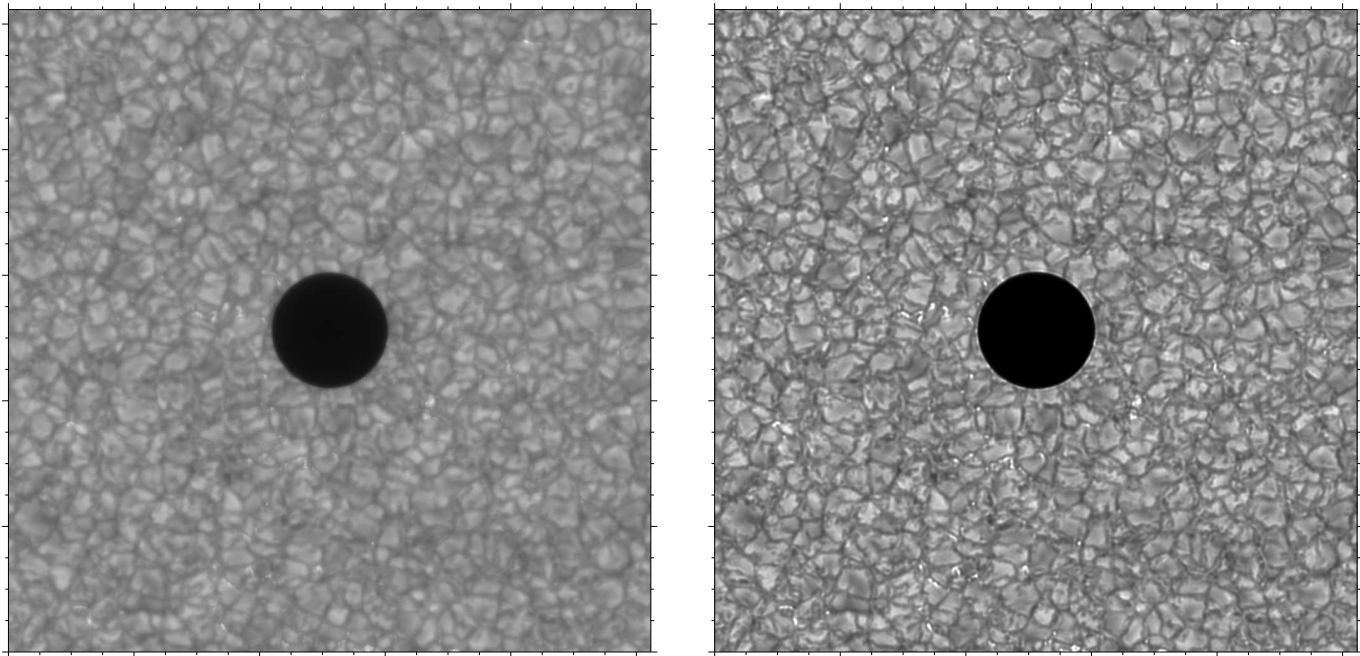


Fig. 3. Observed (*left*) and corrected (*right*) G-band images. Each tick mark corresponds to ~ 2.7 arcsec. The images are cropped to 1024×1024 pixels, such that Mercury is at the center of the FOV. Both the images are plotted on the same gray scale.

1996). This method invokes an iterative process and updates the current estimate of the image by the product of previous deconvolution results and the correlation between re-convolution of the later image and the PSF. The convergence of restoration is checked from the chi-square of the fit which was obtained by comparing the observed data and the re-convolved deconvolution results. The filled circles in Fig. 1 show the azimuthally averaged intensity profile across the Mercury image after the deconvolution. The intensity lies close to zero throughout almost the whole of Mercury’s image, compared to observed values of 7% or higher in units of averaged quiet-Sun intensity. This indicates that the deconvolution is effective in removing the scattered light. In Fig. 3 an observed G-band image is shown on the left and the corresponding restored image on the right. The higher contrast of the restored image is quite marked. Note that both images have been plotted on the same gray-scale (for restored images in other wavelengths we refer to the additional electronic material to the paper; Figs. B.1 and B.2). A halo like structure is seen around the Mercury in the deconvolved image, which could result from Gibb’s effect due to the large intensity variation across Mercury’s limb. We have investigated whether bright points are also affected by comparing the observed and corrected intensity profiles across sample bright points. We have not observed any noticeable signature of Gibb’s effect in bright points which could introduce errors in our contrast analysis.

3. Contrast analysis

The deconvolution of the BFI images leads to significant enhancements of the contrast. This is illustrated by Table 2, which compares the *rms* contrast of the images (excluding Mercury and nearby surroundings) and the intensity contrast, C , of G-band bright points (BPs) ($C = I/I_0 - 1$, where I_0 is the average quiet-Sun intensity) in each filtergram before and after deconvolution. The *rms* contrast is 1.6 to 2.1 times higher in deconvolved images than in the originally observed images. Note that since we are dealing with quiet-Sun data the *rms* contrast of the

Table 2. *rms* contrast of the images and mean BP contrast values obtained before and after deconvolution.

Wavelength (Å)	Observed <i>rms</i>	Observed $\langle C \rangle$	Deconvolved <i>rms</i>	Deconvolved $\langle C \rangle$
3883 (CN)	0.134	0.379	0.218	0.784
4305 (GB)	0.111	0.293	0.192	0.702
4504 (BC)	0.122	0.028	0.215	0.077
5550 (GC)	0.075	0.038	0.158	0.097
6684 (RC)	0.054	0.038	0.111	0.069

image corresponds basically to the granulation contrast, which lies above 20% at two of the observed wavelengths after correction. We also compared the retrieved contrasts with the results obtained from 3-D MHD simulations. By a linear fit to the contrasts obtained at different continuum wavelengths we deduce an *rms* contrast of 0.128 (with a 1σ error of 0.035) at 6302 Å. This value is only 0.017 (i.e. 0.5σ) lower than the granulation contrast of 0.144 at 6302 Å obtained from 3-D radiation MHD simulations by Danilovic et al. (2008).

The BP contrast given in Table 2 also increases after deconvolution of the PSF, by a factor of 1.8 to 2.8. To identify the BPs we used a technique described by Berger et al. (1998) with an additional constraint imposed following Langhans et al. (2004). The combination of these methods secures a more reliable BP selection (Zakharov et al. in prep.). Another way of showing the enhancement in the contrast through the deconvolution, is to plot the G-band intensity versus the blue continuum intensity (BC). Figure 4 displays the well-known (e.g. Berger et al. 1998, Shelyag et al. 2005 and references therein) concentration of data points in two groups: granulation (in black) and BPs (in red). In order to avoid artifacts introduced by the different wavelengths and hence different spatial resolutions of the recorded images, we performed a spatial filtering of the acquired CN, G-band and blue continuum images to set them to a common spatial resolution of 0.22 arcsec, which corresponds to the diffraction limit of SOT at $\lambda = 450.4$ nm.

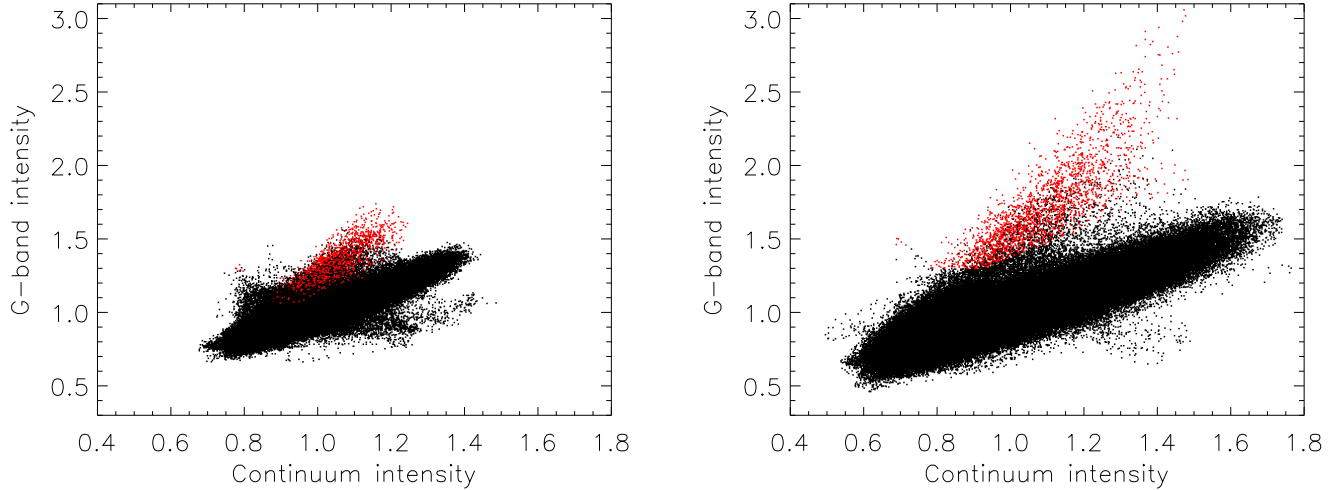


Fig. 4. Distribution of the G-band intensity versus blue continuum intensity. Red points correspond to BPs, black dots to the remaining features. All intensity values are normalized to the average intensity of that wavelength band. Left frame: before and right frame: after deconvolution of the PSF.

The mean BP contrast in the CN-band is higher than in the G-band, both in the original data as well as in the deconvolved data by a factor of 1.29 and 1.12, respectively. This finding qualitatively confirms the theoretical predictions of Berdyugina et al. (2003) and ground-based imaging results (Rutten et al. 2001, Zakharov et al. 2007). Figure 5 displays the dependence of the ratio C_{CN}/C_{GB} on the G-band intensity (after PSF deconvolution), where C_{CN} and C_{GB} are the contrasts of the respective bands as defined earlier in this section. In order to obtain the right slope, we bin together points with similar G-band intensities such that each bin contains 20 intensity values. The solid line represents a linear regression fit and the error bars are plotted for $\pm 1\sigma$ deviations due to the uncertainty in the regression gradient. From this analysis we obtain a statistically significant negative slope of 0.054, which indicates that brighter BPs tends to have more similar CN-band and G-band contrasts. This is in qualitative agreement with the result of Zakharov et al. (2007).

4. Conclusions

Filtergrams recorded by the Hinode/SOT broad-band imager were used to analyze the contrast of the bright points and the granulation in various wavelength bands. The observed images were deconvolved with the retrieved PSF of the instrument in order to obtain the original intensities. The retrieved images are nearly free from scattered light and show a 1.6 - 2.1 times higher *rms* contrast than the untreated images, while the contrast of BPs increases by a factor of 1.8 - 2.8. The stronger enhancement of the BP contrast is due to their smaller size than granules, which are dominantly responsible for the *rms* contrast of the whole image.

Acknowledgements. Hinode is a Japanese mission developed and launched by ISAS/JAXA, with NAOJ as domestic partner and NASA and STFC (UK) as international partners. It is operated by these agencies in co-operation with ESA and NSC (Norway). We would like to thank the referee for useful suggestions. This work has been (partially) supported by the WCU grant (No. R31-10016) funded by the Korean Ministry of Education, Science and Technology.

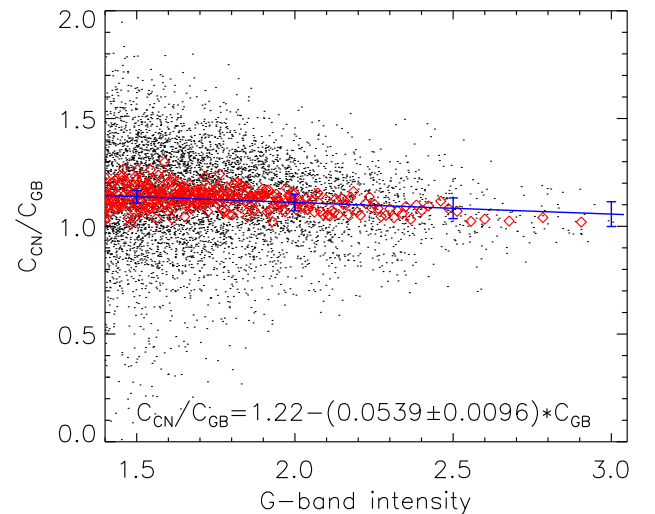


Fig. 5. Ratio of BP contrasts in the CN-band and in the G-band versus the G-band intensity, normalized to its mean. Individual data points are shown as black dots and red symbols are for the binned data. The solid blue line is a linear regression fit to the binned data and the error bars for $\pm 1\sigma$ uncertainty in the gradient.

References

- Berdyugina, S. V., Solanki, S. K., Frutiger, C. 2003, *A&A*, 412, 513
- Berger, T. E., Löfdahl, M. G., Shine, R. A., Title, A. M. 1998, *ApJ*, 506, 439
- Danilovic, S., Gandorfer, A., Lagg, A., Schüssler, M., Solanki, S. K., Vögler, A., Katsukawa, Y., Tsuneta, S. 2008, *A&A*, 484, L17
- Kosugi, T., Matsuzaki, K., Sakao, T., et al. 2008, *Sol. Phys.*, 243, 3
- Lane, R. G. 1996, 2004, *J. Opt. Soc. Am.*, 13, 1992
- Langhans, K., Schmidt, W., Rimmele, T. 2004, *A&A*, 423, L1147
- Mathew, S. K., Martínez Pillet, V., Solanki, S. K., Krivova, N. A. 2007, *A&A*, 465, 291
- Richardson, W. H. 1972, *J. Opt. Soc. Am.*, 62, 55
- Rutten, R. J., Kiselman, D., Rouppe van der Voort, L., Plez, B. 2001, in *Advanced solar polarimetry – theory, observation, and instrumentation*, ed. M. Sigwarth, *ASP Conf. Ser.*, 236, 445

- Shelyag, S., Schüssler, M., Solanki, S. K., Berdyugina, S. V., Vögler, A. 2005, A&A, 427, 335
- Suemastu, Y., Tsuneta, S., Ichimoto, K., et al. 2008, Sol. Phys., 249, 197
- Tsuneta, S., Ichimoto, K., Katsukawa, Y., et al. 2008, Sol. Phys., 249, 167
- Wedemeyer-Bhöhm, S. 2008, A&A, 487, 399
- Zakharov, V., Gandorfer, A., Solanki, S. K., Löfdahl, M. 2007, A&A, 461, 695